Inorganic Chemistry

pubs.acs.org/IC Article

Dysprosium and Holmium Vanadate Nanoprobes as High-Performance Contrast Agents for High-Field Magnetic Resonance and Computed Tomography Imaging

Elisabet Gómez-Gónzalez, Nuria O. Núñez, Carlos Caro, Maria L. García-Martín, Yilian Fernández-Afonso, Jesús M. de la Fuente, Marcin Balcerzyk, and Manuel Ocaña*

Cite This: *Inorg. Chem.* 2021, 60, 152−160 Read Online

ACCESS | Metrics & More | Article Recommendations

ABSTRACT: We describe a wet chemical method for the synthesis of uniform and well-dispersed dysprosium vanadate ($DyVO_4$) and holmium vanadate ($HoVO_4$) nanoparticles with an almost spherical shape and a mean size of ∼60 nm and their functionalization with poly(acrylic acid). The transverse magnetic relaxivity of both systems at 9.4 T is analyzed on the basis of magnetic susceptibility and magnetization measurements in order to evaluate their potential for application as high-field MRI contrast agents. In addition, the X-ray attenuation properties of these systems are also studied to determine their capabilities as computed tomography contrast agent. Finally, the colloidal stability under physiological pH conditions and the cytotoxicity of the functionalized NPs are also addressed to assess their suitability for bioimaging applications.

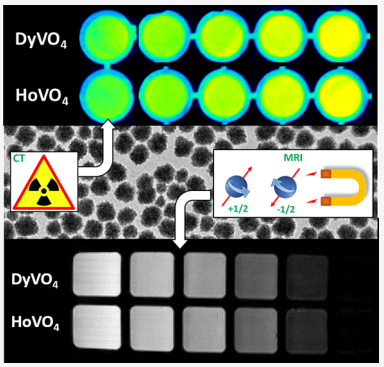

INTRODUCTION

MRI is a noninvasive imaging technique having a high penetration power that is commonly used for the visualization of organs and tissues in the medical diagnosis field. The contrast in MRIs is based on the differences in the density of protons between different tissues and the differences in their longitudinal (T_1) and transverse (T_2) relaxation times. The sensitivity of this technique is relatively low because the difference in contrast between normal and abnormal tissues is generally low. To increase such contrast, external probes (contrast agents, CAs) are frequently used, which are sorted in two types: T_1 CAs, which are commonly called positive contrast agents due to the signal enhancement they produce on T_1-weighted images, and T_2, or negative, CAs, which produce darkening on T_2-weighted images. The capacity of a substance to act as negative or positive MRI contrast agent is given by their longitudinal (r_1) and transverse (r_2) relaxivity values obtained from the $1/T_{1,2}$ versus CA concentration plot. Thus, positive CAs are those having a low r_2/r_1 value (between 1 and 3), whereas high r_2/r_1 values (>10) are associated with negative CAs. Finally, when r_2/r_1 results in an intermediate value (between 3 and 10), the substance may act as both positive and negative CA.[1] Currently, most medical tests are conducted with equipment working at rather low magnetic fields (0.5−1 T), using superparamagnetic iron oxide (SPIO) nanoparticles (NPs) as negative CAs[2] and Gd^{3+} chelates as positive CAs,[3] respectively.

One of the most novel research lines in this field is aimed at increasing the sensitivity of images and reducing their acquisition time by using magnets much more powerful (from 7 to 9 T) than those currently used in clinics (<3 T).[4] Unfortunately, the efficiency of Gd^{3+} chelates is optimum for a magnetic field strength <1 T, whereas the magnetization of SPIO saturates at about 1.5 T, which limits their efficacy as an MRI CA at higher fields.[5] Therefore, the development of new CAs suitable for this purpose is required. Among the possible alternatives, Dy^{3+} and Ho^{3+} compounds are considered as the best candidates since both cations present the highest magnetic moment among lanthanides, which favors their transverse relaxivity.[5] Due to their novelty, the current research on these high-field CAs is scarce. The few previous reports on this subject deal with different Ho^{3+} or Dy^{3+} complexes,[6] whose main drawbacks are their short circulation times and their scarce ability for targeting. In order to minimize these inconveniences, the use of CAs consisting of NPs (≤100 nm) has been proposed,[7] since by controlling their size it is possible to control circulation time and elimination pathways.[8] In addition, NPs can

Received: September 1, 2020
Published: November 17, 2020

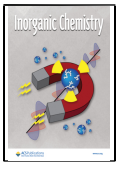

https://dx.doi.org/10.1021/acs.inorgchem.0c02601
Inorg. Chem. 2021, 60, 152−160

be easily functionalized so that they can be concentrated into the region of interest,[2] preventing their dissemination to other areas of the organism. For these reasons, several CAs based on Ho^{3+}- or Dy^{3+}-containing NPs[7,9,10] have been also investigated, most of which are based on different kinds of Dy^{3+} or Ho^{3+} fluorides.[9,10] It must be mentioned that the chemical stability of lanthanide fluorides in the aqueous medium, and therefore in the physiological medium in which they have to be used, is limited.[11] Therefore, the development of Dy^{3+}- and Ho^{3+}-containing NPs based on matrices other than fluorides is attractive. Interesting alternatives are Dy^{3+} or Ho^{3+} vanadates, since different kinds of lanthanide-based vanadate NPs have been shown to be excellent candidates for bioimaging,[12,13] including MRI at low field, as in the case of $GdVO_4$.[14] In spite of this, to the best of our knowledge, the performance of Dy or Ho vanadate NPs as high-field MRI CAs has never been addressed. It is worth mentioning that because of the high atomic number of these lanthanide cations these probes are also expected to show a high capability for X-ray attenuation, which confer on them an additional functionality as CA for X-ray computed tomography (CT).[13]

It is important to note that for *in vivo* biomedical applications, NPs must meet some important requirements such as (i) homogeneous particle size and shape, since these characteristics affect the interactions of the particles with the cells (internalization, proliferation, adhesion, etc.), (ii) particle size between about 20 and 100 nm to control circulation time, since smaller particles are quickly eliminated through the kidney and the larger ones are eliminated by the reticuloendothelial system, the spleen, or the liver, (iii) aggregation in the physiological environment should be avoided to meet the above size criteria, and (iv) lack of toxicity. However, most of the few reported procedures for the synthesis of Dy or Ho vanadate NPs yield particles with at least one dimension much higher than 100 nm,[15−19] NPs with broad size distribution,[20] or with an apparently high degree of aggregation,[18,21] which precludes their use as MRI CAs.

In this work, we have developed a wet chemical method for the synthesis of uniform and well-dispersed dysprosium vanadate ($DyVO_4$) and holmium vanadate ($HoVO_4$) NPs with an almost spherical shape and a mean size of ∼60 nm. A method is also reported for their functionalization with poly(acrylic acid) (PAA) molecules to render them colloidally stable under physiological pH conditions. The magnetic relaxivity of both systems at 9.4 T has been measured in order to evaluate their potential applications as high-field MRI CAs. In addition, the magnetic susceptibility and magnetization of these of CAs has been analyzed in order to explain their differences in magnetic relaxation behavior. An X-ray attenuation study was also undertaken to determine the suitability of the probes as CT CA. Finally, the cytotoxicity of the functionalized NPs is evaluated to assess their suitability for bioimaging applications.

EXPERIMENTAL SECTION

Reagents. Dysprosium acetate hydrate ($Dy(OAc)_3$, $(CH_3CO_2)_3Dy{\cdot}xH_2O$, 99.9%, Sigma-Aldrich), holmium acetate hydrate ($Ho(OAc)_3$, $(CH_3CO_2)_3Ho{\cdot}xH_2O$, 99.99%, Sigma-Aldrich), sodium orthovanadate (Na_3VO_4, Sigma-Aldrich, 99.98%), ethylene glycol (EG, $C_2H_6O_2$, 99.8%, Sigma-Aldrich), poly(acrylic acid) (PAA, average M_w ∼ 1800, Sigma-Aldrich) 2-morpholinoethanesulfonic acid (MES, Sigma-Aldrich, 99%), and iohexol (≥95%, Sigma-Aldrich) were used as received.

Nanoparticle Synthesis. For the synthesis of uniform dysprosium vanadate NPs, we adapted a polyol-based method, previously developed by us to fabricate gadolinium vanadate,[14] which has to be slightly modified in order to obtain the desired $DyVO_4$ NPs. Essentially, this method involves the aging (at 120 °C for 20 h) of solutions containing $Dy(OAc)_3$ (0.02 M) and Na_3VO_4 (0.1 M) using an EG/H_2O mixture (4:1 by volume) as the solvent. The experimental procedure was as follows. The Dy precursor was dissolved in the EG−H_2O mixture (1 mL of H_2O + 1.5 mL of EG). In a separate vial, Na_3VO_4 was dissolved in EG (2.5 mL) at ∼80 °C under magnetic stirring to facilitate dissolution. After cooling down to room temperature, this solution was added under magnetic stirring to the Dy-containing one. The resulting mixture was finally aged in a conventional oven preheated at the desired temperature under the conditions described above. The obtained precipitate was cooled down to room temperature and washed twice with ethanol and once with double-distilled water. The as-purified NPs were finally dispersed in distilled water or dried at 50 °C for some analyses.

For the functionalization of the $DyVO_4$ NPs, we used the experimental procedure just described but introducing a certain amount (2 mg mL^{-1}, referred to the total volume of the final solution) of PAA into the starting Dy^{3+}-containing solution. This procedure was also used for the synthesis of the $HoVO_4$ NPs functionalized with PAA, obviously replacing $Dy(OAc)_3$ by $Ho(OAc)_3$.

Characterization Techniques. Transmission electron microscopy (TEM, Phillips 200CM) was used to assess particle shapes. For the TEM analyses, a droplet of an aqueous suspension of the samples on a copper grid coated with a transparent polymer. Particle size distributions were evaluated by counting about one hundred of particles on the TEM micrographs, using the free software *ImageJ*.

To obtain information on colloidal stability of the NPs in aqueous suspension (0.5 mg·mL^{-1}), dynamic light scattering (DLS) measurements were performed using a Malvern Zetasizer Nano-ZS90 equipment.

X-ray powder diffraction (XRD) was used for phase identification. The patterns were obtained using a Panalytical, X'Pert Pro diffractometer (Cu Kα) with an X-Celerator detector with a 2θ step width of 0.02°, and 10 s counting time.

The infrared spectra (FTIR) of powdered samples diluted in KBr pellets were recorded in a Jasco FT/IR-6200 Fourier transform spectrometer. Thermogravimetric analyses (TGA) were conducted in air atmosphere, at a heating rate of 10 °C min^{-1}, using a Q600TA Instrument.

X-ray attenuation properties of our NPs and iohexol, a commercial iodine-based CT contrast agent used for comparative purposes, were evaluated for aqueous suspensions having different CAs contents. For this purpose, 200 μL of each suspension were placed in a multiwell microplate with a Milli-Q water sample for calibration. CT images were acquired with a NanoSPECT/CT (Bioscan, USA; currently Mediso, Hungary). Acquisition parameters were as follows: 65 kVp operation potential, 106 mA current, 1500 ms of exposure time per projection, and 240 projections per rotation. The image length was 12 cm with pitch of 1, and the acquisition time was 21 min. The image was reconstructed with VivoQuant image processing software (Invicro, USA) with the Exact Cone Beam Filtered Back Projection algorithm and Shepp Logan 98% filter. The resulting image pixel size was uniform in three dimensions at 0.2 mm. Images were analyzed with PMOD 4.1 software (PMOD Technologies LLC, Switzerland) in a gray scale (or cold scale). Spherical volumes of interest (VOIs) of 2 mm radius were made within each sample to calculate the X-ray attenuation (HU) for each suspension. Average values of Milli-Q water and solutions were used to calculate Hounsfield units in the images, with attenuations being 0 and −1000 HU for water and air, respectively.

Transverse ^1H relaxation times (T_2) were determined for different concentrations of Dy^{3+} or Ho^{3+} at 298 K using a Bruker Biospec operating at 9.4 T. T_2 was obtained using the Carl−Purcell−Meiboom−Gill (CPMG) sequence. The transverse relaxivity (r_2) was obtained from the slopes of the linear fits of $1/T_2$ versus the concentration of Dy^{3+} or Ho^{3+}.

Sample preparation for magnetic measurements was performed by placing a known volume (100 μL) of the aqueous suspensions into a piece of cotton wool and allowing it to dry at room temperature. The

https://dx.doi.org/10.1021/acs.inorgchem.0c02601
Inorg. Chem. 2021, 60, 152−160

dried wool was then placed inside a gelatin capsule for the magnetic characterization. Magnetic measurements were performed in a Quantum Design (USA) MPMS-XL SQUID magnetometer. Temperature dependence of the alternating current (ac) magnetic susceptibility was recorded from 2 to 300 K, at a frequency of 11 Hz and a magnetic field amplitude of 4.1 Oe. Field-dependent magnetization was recorded at 5 and 300 K in the field ranges between −20 and 20 kOe, on both samples.

Cytotoxicity was evaluated in PC3 (human prostate adenocarcinoma) cells using the MTT assay.[22] Briefly, cells were plated at a density of 1×10^4 cells/well in a 96-well plate at 37 °C in 5% CO_2 atmosphere (100 μL per well, number of repetitions = 5). After 24 h of culture, the medium in the wells was replaced with fresh medium containing NPs in varying concentrations from 9 to 300 μg/mL. After 24 h, the supernatant of each well was replaced by 100 μL of fresh medium with 3-[4,5-dimethylthiazol-2-yl]-2,5-diphenyl tetrazolium bromide (MTT) (0.5 mg/mL). After 2 h of incubation at 37 °C and 5% CO_2, the medium was removed and the formazan crystals were solubilized with 200 μL of DMSO, and the solution was vigorously mixed to dissolve the reacted dye. The absorbance of each well was read on a microplate reader (Dynatech MR7000 instruments) at 550 nm. The relative cell viability (%) and its error related to control wells containing cell culture medium without NPs were calculated by the equations:

$$\text{RCV}\ (\%) = \left(\frac{[\text{Abs}]\text{test} - [\text{Abs}]\text{Pos. Ctrl}}{[\text{Abs}]\text{Neg. Ctrl} - [\text{Abs}][\text{Abs}]\text{test} - [\text{Abs}]\text{Pos. Ctrl}}\right) \times 100 \quad (1)$$

$$\text{Error}\ (\%) = \text{RCV test} \times \sqrt{\left(\frac{[\sigma]\text{test}}{[\text{Abs}]\text{test}}\right)^2 + \left(\frac{[\sigma]\text{control}}{[\text{Abs}]\text{control}}\right)^2} \quad (2)$$

where σ is the standard deviation. Triton X-100 was added to the positive control wells. Statistical analysis was performed using the SPSS package (v20, SPSS Inc., Chicago, Illinois). Cell viability values are shown as mean ± standard deviation (SD). Student's *t*-test or one-way analysis of variance (ANOVA) were used to determine significant differences. The level of significance was set at $p < 0.05$.

RESULTS AND DISCUSSION

Nanoparticle Synthesis and Characterization. The particles obtained as described in the Experimental Section in the absence of PAA for the dysprosium system, consisted of $DyVO_4$ with tetragonal crystalline structure (Figure 1).

As observed in the TEM micrograph shown in Figure 2a, they showed an almost spherical shape having a mean size of 60 nm (standard deviation, σ = 8; Figure 2b). This value was very similar to the mean hydrodynamic diameter (D_h) value (81 nm) obtained for these particles in water suspensions (pH 6.9; Figure 2c) indicating that the NPs were free of aggregation. Nevertheless, we also measured the DLS curve for these NPs suspended in a physiological pH simulator (50 mM MES, pH 6.5) in order to assess the colloidal stability criterion required for *in vivo* bioapplications, finding that the $D_h$value exhibited an substantial increase (609 nm) under these conditions (Figure 2c), which make these NPs not appropriate for such applications.

Aiming to improve the colloidal stability, we decided to functionalize the NPs surface with PAA molecules, which have been shown to be efficient dispersing agents for other $LnVO_4$ (Ln = La, Lu, and Gd) systems.[12−14] For that purpose, we performed the synthesis under similar conditions to those involved in the case of the NPs shown in Figure 2a, but adding a certain amount (2 mg mL^{-1}) to the Dy precursor solution. In this way, NPs with the same tetragonal structure as $DyVO_4$

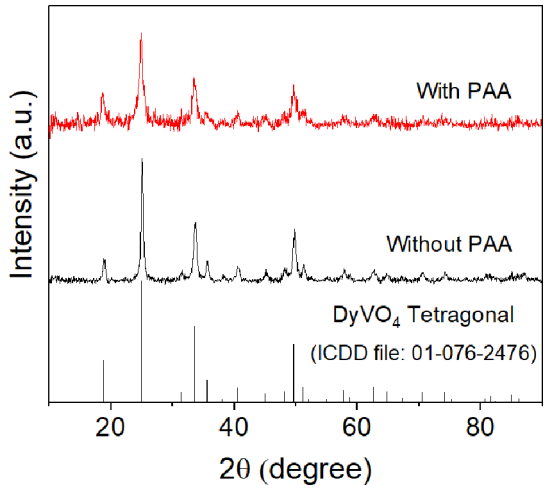

Figure 1. X-ray diffraction patterns of the particles synthesized by the aging (at 120 °C for 20 h in the absence or the presence of 2 mg mL^{-1} of PAA) of solutions containing $DyAc_3$ (0.02 M) and Na_3VO_4 (0.1 M) in EG/H_2O mixtures (volumetric ratio = 4/1). Reference pattern: International Centre for Diffraction Data (ICDD) File 01-076-2476.

(Figure 1) and similar shape (Figure 2d) and size (66 nm, σ = 10) (Figure 2e) were obtained. More interestingly, the hydrodynamic diameter of the nanospheres in MES (pH 6.5) medium was very similar (D_h = 94 nm) to that in water (pH 5.7, D_h = 87 nm; Figure 2f), in both cases being only slightly higher than the mean particle size obtained from TEM observations. This finding manifests the pursued beneficial effect of PAA on the colloidal stability of the NPs dispersion in physiological buffer, which might be ascribed to the adsorption of PAA molecules on the NPs surface.[13] In agreement with this suggestion are the *Z* potential measurements carried out for aqueous suspensions (pH 5.7) of the NPs. Thus, it was found that *Z* potential varied from −37 mV for the NPs obtained in the absence of PAA to 49 mV for those obtained in the presence of this additive. Such an increase of surface charge should be a consequence of the presence of the PAA molecules on the NPs surface. The incorporation of PAA to the NPs was confirmed by comparison of the FTIR spectra of the NPs synthesized in the absence or presence of PAA (Figure 3, top).

Thus, in the last case ($DyVO_4$@PAA), the spectrum clearly displayed the absorptions due to vibrational modes of $DyVO_4$ (<1000 cm^{-1}) and adsorbed water (around 3400 and 1600 cm^{-1}), along with bands between 1400 and 1550 cm^{-1}, which are not detected in the spectrum of the particles obtained in the absence of PAA. Such features can be attributed to the symmetric and asymmetric stretching vibrational modes of the PAA carboxylate anions, respectively.[23] For quantification of the amount of adsorbed PAA, TGA analyses were performed. As observed in Figure 3 (bottom), the TGA curve obtained in the absence of PAA only showed a weight loss, mainly taking place in the 25−300 °C (~4.5%) temperature range, due to the release of adsorbed water. For the sample obtained in the presence of PAA ($DyVO_4$@PAA), such water release was also detected (~7%, in this case) followed by an additional weight loss (~9%) in the 300−800 °C range, which can be attributed to the decomposition of the PAA species. An additional advantage of the presence of such species on the $DyVO_4$ NPs surface is that they provide them with carboxylate functional groups suitable for a further bioconjugation, which is eventually needed for

https://dx.doi.org/10.1021/acs.inorgchem.0c02601
Inorg. Chem. 2021, 60, 152−160

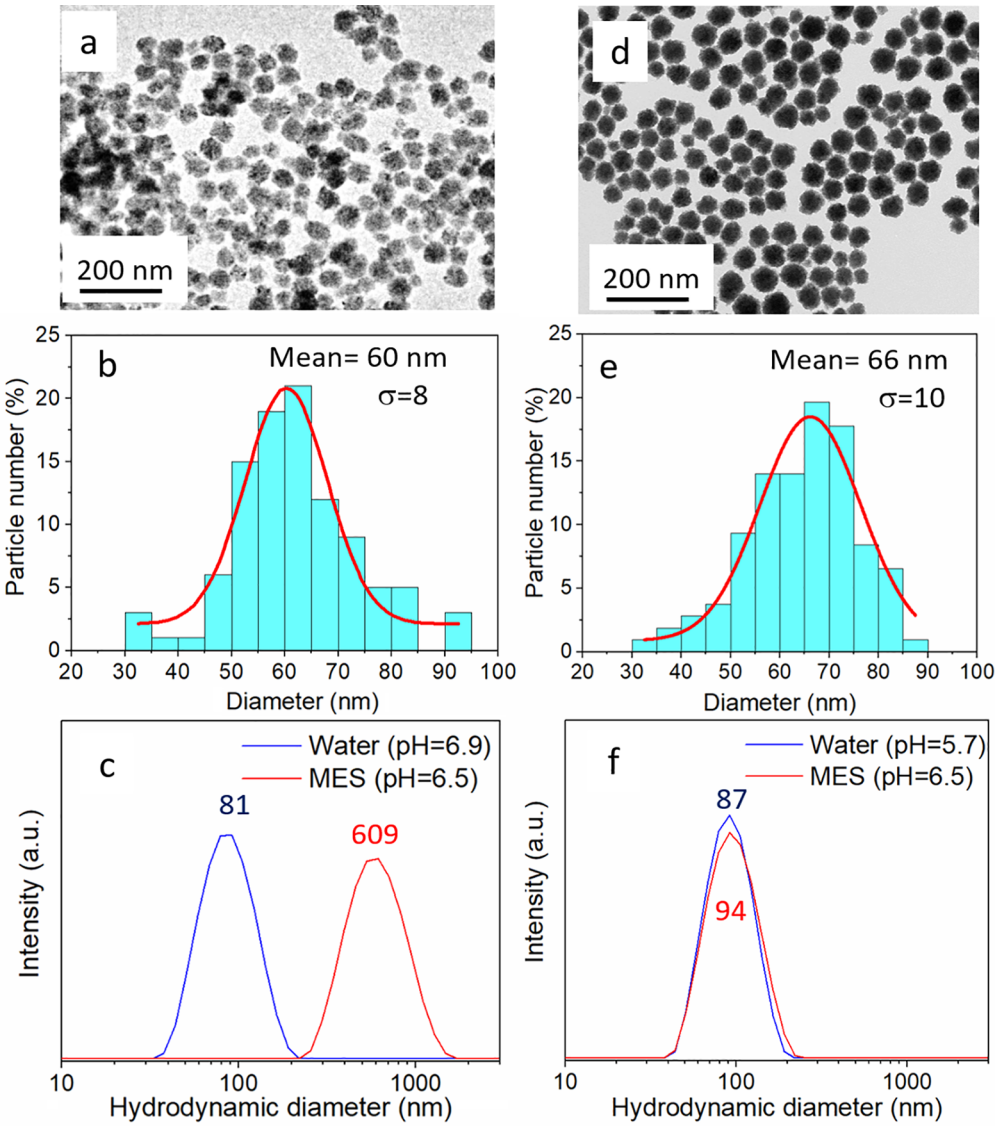

Figure 2. TEM images (a, d), particle size histograms (b, e), and DLS curves in water and MES solutions (c, f) of the particles synthesized by the aging (at 120 °C for 20 h) of solutions containing $DyAc_3$ (0.02 M) and Na_3VO_4 (0.1 M) in EG/H_2O mixtures (volumetric ratio = 4/1) in the absence (a–c) or the presence (d–f) of 2 mg mL^{-1} of PAA.

many processes involved in their potential bioapplications, such as targeting.[24]

Because of the success of the latter procedure for the synthesis of colloidally stable $DyVO_4$ NPs, it was extended for the synthesis and PAA functionalization of $HoVO_4$ by replacing the Dy^{3+} precursor by $Ho(OAc)_3$. Spherical NPs were also obtained in this case (Figure 4a), which consisted of tetragonal $HoVO_4$ (Figure 4b). The mean diameter of these NPs (Figure 4c) was similar (65 nm, $\sigma = 6$) to that of the $DyVO_4$ system and close to their D_h values, both in water (pH 6.2, 74 nm) and MES (pH 6.5, 80 nm) suspensions (Figure 4d), revealing their colloidal stability in such media. As in the $DyVO_4$ case, the presence of PAA on the NPs surface was confirmed by carboxylate bands (from 1400 to 1500 cm^{-1}) in the FTIR spectrum (Figure 5, top) of the functionalized $HoVO_4$ sample ($HoVO_4$@PAA) and by a weight loss of ~9.5% in the 300–800 °C range of its TGA curve (Figure 5, bottom) corresponding to the release of PAA.

X-ray Attenuation Properties. For the evaluation of the X-ray attenuation capability of the $DyVO_4$ and $HoVO_4$ NPs functionalized with PAA, several aqueous suspensions containing different CAs content were prepared. The X-ray attenuation phantom images obtained for these systems along with those obtained for iohexol, a commercial iodine-based CT contrast agents used for comparative purposes, are shown in Figure 6 (top).

It can be clearly observed that for both $DyVO_4$ and $HoVO_4$ the contrast produced at any NPs concentration is higher than that corresponding to iohexol, suggesting the superior performance of our NPs as a CT contrast agent. A quantification of this behavior is given in Figure 6 (bottom), where the X-ray attenuation values have been plotted in Hounsfield units (HU) as a function of the CA concentration. As expected, when increasing the CA concentration, a linear increase of the HU values was detected. More interestingly, the slope of the obtained straight line for our systems was very similar (29.6 HU/mg cm^{-3} for $DyVO_4$ and 29.1 HU/mg cm^{-3} for $HoVO_4$) and much higher than that for iohexol (12.7 HU/mg cm^{-3}), an iodine-based probe, indicating that a lower dose of our Dy- or Ho-based CA is required to obtain a similar contrast, which should be favorable for the patient. The higher X-ray attenuation

https://dx.doi.org/10.1021/acs.inorgchem.0c02601
Inorg. Chem. 2021, 60, 152–160

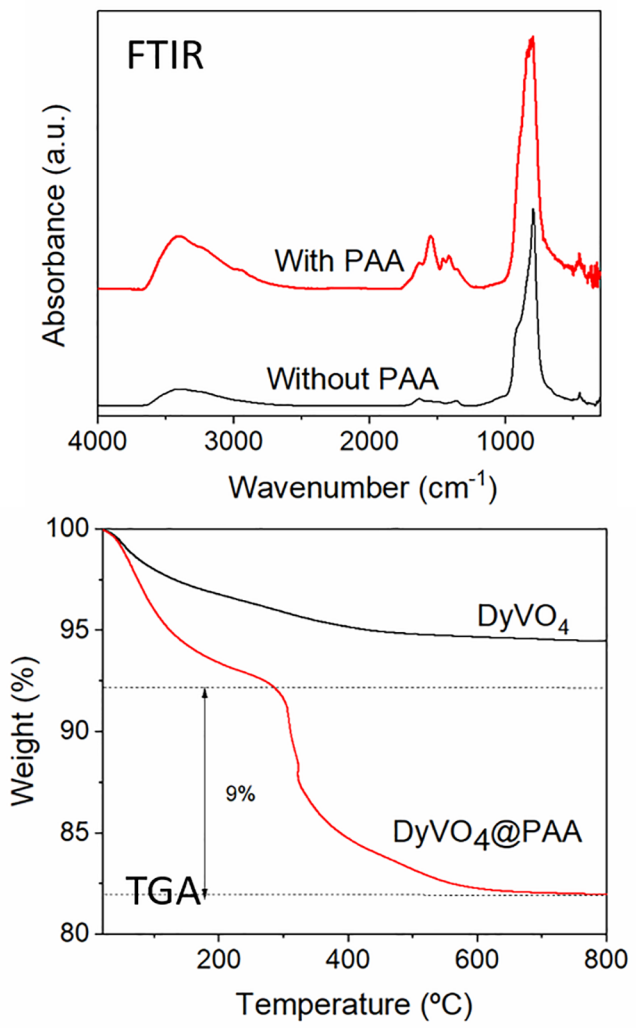

Figure 3. FTIR spectra (top) and TGA curves (bottom) obtained for the particles synthesized by the aging (at 120 °C for 20 h in the absence or the presence of 2 mg mL^{-1} of PAA) of solutions containing $DyAc_3$ (0.02 M) and Na_3VO_4 (0.1 M) in EG/H_2O mixtures (volumetric ratio = 4/1).

capacity of our CAs when compared with iohexol can be attributed to the higher atomic number of Dy ($Z = 66$) and Ho ($Z = 67$), as compared with that of I ($Z = 53$), since it is well-known that the X-ray attenuation coefficient increases with the fourth power of Z.[25] The similar Z value for Dy and Ho therefore justifies the similar X-ray attenuation properties of the Dy- and Ho-based samples.

Magnetic properties. The T_2-weighted MRI phantom images obtained at 9.4 T for the PAA-functionalized $DyVO_4$ and $HoVO_4$ NPs are shown in Figure 7 (top). In this figure, a darkening of the MRI images can be clearly observed as increasing concentration of both kind of NPs in the aqueous suspensions, manifesting that they behave as effective negative CAs. The r_2 values obtained from the $1/T_2$ plot versus lanthanide concentration (Figure 7, bottom) were slightly higher (460 mM^{-1} s^{-1}) for $DyVO_4$ than those for $HoVO_4$ (424 mM^{-1} s^{-1}), indicating a better performance of the former as a CA for high-field MRI.

To explain such behavior, the temperature dependence of the magnetic susceptibility, $\chi(T)$, and the field-dependent magnetization, $M(H)$, at both 5 and 300 K were recorded for both

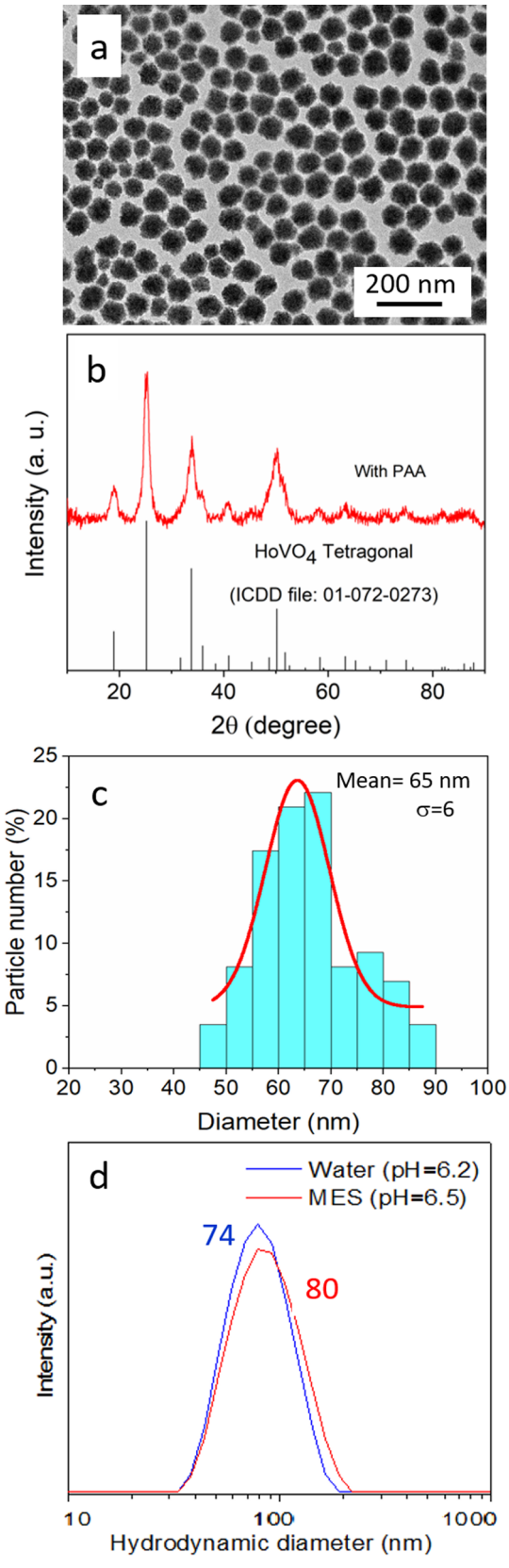

Figure 4. (a) TEM image, (b) particle size histogram, (c) DLS curve, and (d) X-ray diffraction pattern of the particles synthesized by the aging (at 120 °C for 20 h) of solutions containing $HoAc_3$ (0.02 M), Na_3VO_4 (0.1 M), and PAA (2 mg/mL) in EG/H_2O mixtures (volumetric ratio = 4/1).

https://dx.doi.org/10.1021/acs.inorgchem.0c02601
Inorg. Chem. 2021, 60, 152−160

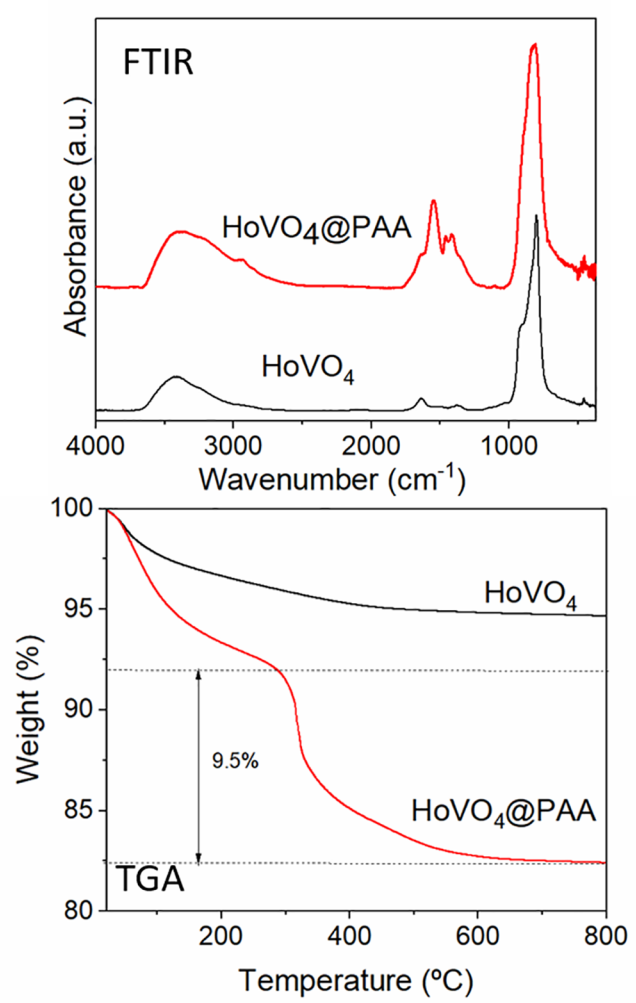

Figure 5. FTIR spectra (top) and TGA curves (bottom) obtained for the particles synthesized by the aging (at 120 °C for 20 h in the absence or the presence of 2 mg mL^{-1} of PAA) of solutions containing $HoAc_3$ (0.02 M) and Na_3VO_4 (0.1 M) in EG/H_2O mixtures (volumetric ratio = 4/1).

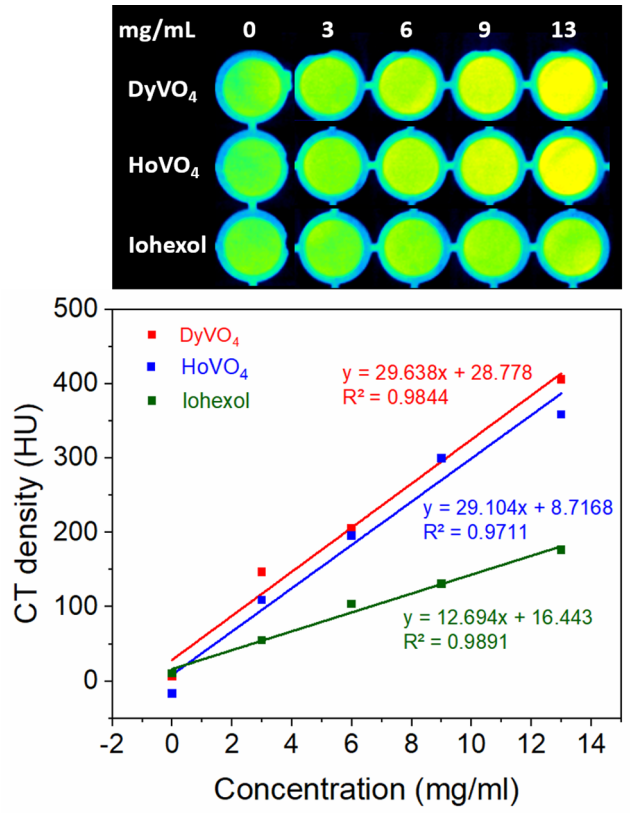

Figure 6. X-ray attenuation phantom images (top) and Hounsfield units (HU) values (bottom) obtained for iohexol and the $DyVO_4$ and $HoVO_4$ NPs functionalized with PAA at different concentrations in water.

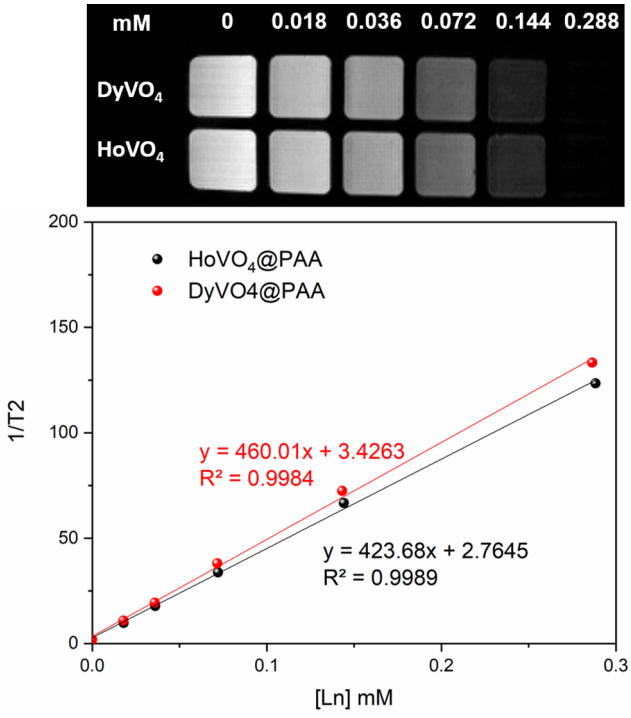

Figure 7. T_2-weighted phantom images (top) and relaxivities (bottom) obtained for the $DyVO_4$ and $HoVO_4$ NPs functionalized with PAA.

systems. As shown in Figure 8a,b, a Curie law behavior in $\chi'(T)$ with negligible χ'' in the whole temperature range was observed for both samples, which is typical of paramagnetic materials, as expected for Dy^{3+} and Ho^{3+} MRI CAs. Such behavior was confirmed by the magnetization curves measured at 5 K (Figure 8c) since no hysteresis (both coercivity and remanence were negligible) was detected. More interestingly, M values were higher for the $DyVO_4$ sample (39 emu/g at 20 kOe) than that for $HoVO_4$ (32.5 emu/g at 20 kOe, Figure 8c), which explains the higher r_2 value for the former because this magnitude is proportional to magnetization[16] for Ln-based NPs, in a quadratic way for the outer sphere regime or in a linear one for the static dephasing regime. It is known that several factors affect the magnetization of paramagnetic Dy^{3+}- and Ho^{3+}-containing samples such as the magnetic moment of such cations and the NPs morphology and size. Thus, the magnetization of these cations increases with the square of their magnetic moment,[26] whereas it has been shown that magnetization is higher for NPs with high shape anisotropy.[27] Finally, lower magnetization is expected for very small NPs due to "spin-canting effects". In this phenomenon, spins located near the surface tend to be slightly tilted (i.e., canted spins) resulting

https://dx.doi.org/10.1021/acs.inorgchem.0c02601
Inorg. Chem. 2021, 60, 152−160

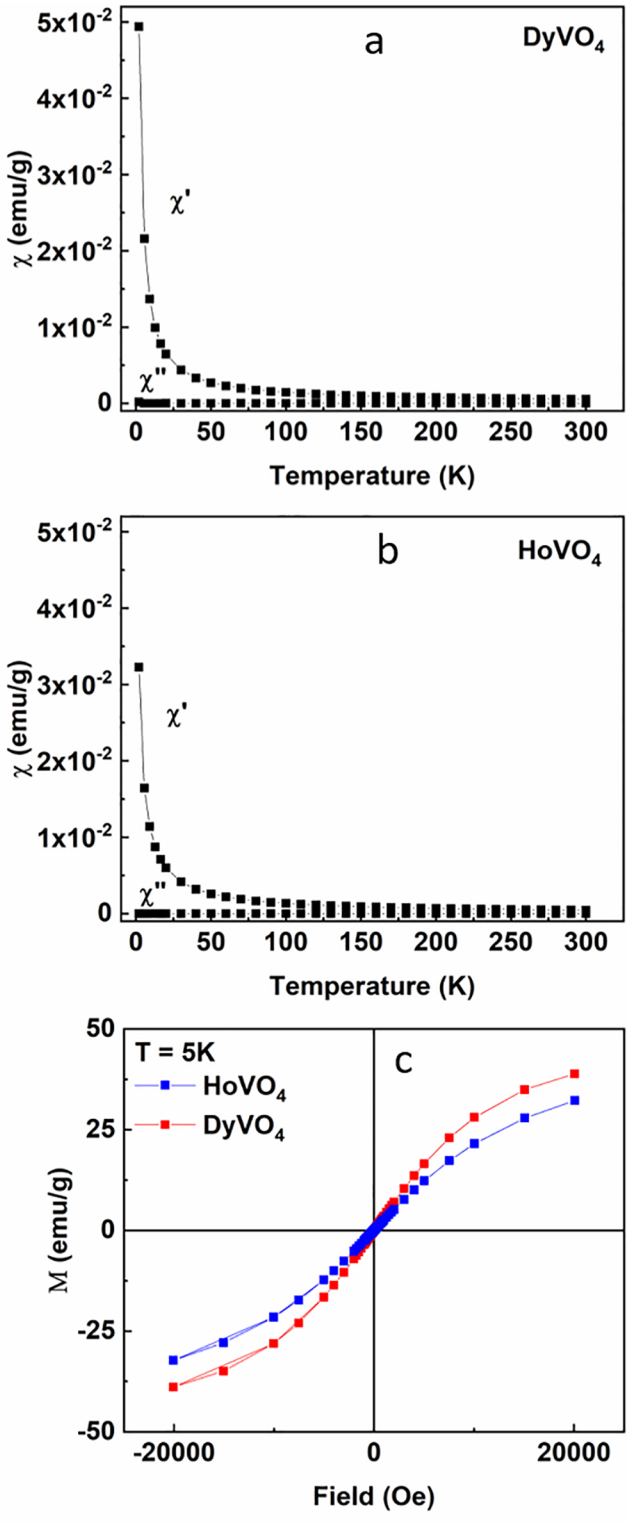

Figure 8. Temperature dependence of the ac magnetic susceptibility recorded for the DyVO4 (a) and $HoVO_4$ (b) NPs functionalized with PAA. Field-dependent magnetization recorded at 5 K (c) for the same samples.

in a lower magnetization value. As the surface-to-volume ratio increases with decreasing NP size, the proportion of canted spins increases, producing an overall lower magnetization.[28] Since particle shape and size are very similar for both systems, the higher r_2 value of our $DyVO_4$ system when compared to that of the $HoVO_4$ one may be ascribed to the slightly higher magnetic moment of Dy^{3+} (~10.63 μ_B) in comparison with that of Ho^{3+} (10.60 μ_B).[10]

It should be noted that a strict comparison of transverse relaxivity data for different systems is only possible if they have been measured at the same magnetic field strength for particles of the same size, owing to the dependence of such magnitude on these parameters. Taking this into account, we have compared the value or r_2 for our samples with those reported in literature for Dy- and Ho-based CAs measured at the same field (9.4 T). We found that our values are clearly higher (>400 mM^{-1} s^{-1}) than most of those previously reported (≤200 mM^{-1} s^{-1}),[9,28] which indicates the superior performance of the here developed CAs for high-field MRI imaging. The only found systems having higher r_2 values were our already reported DyF_3 and HoF_3 nanorhombuses (494−600 mM^{-1} s^{-1}), which have one dimension above 100 nm[10] and, therefore are less suitable for *in vivo* applications than the $DyVO_4$ and $HoVO_4$ NPs here studied.

Cell Viability. The potential cytotoxicity of the $DyVO_4$ and $HoVO_4$ probes was finally evaluated using the MTT assay and the PC3 cell line. As shown in Figure 9, cell survival was above

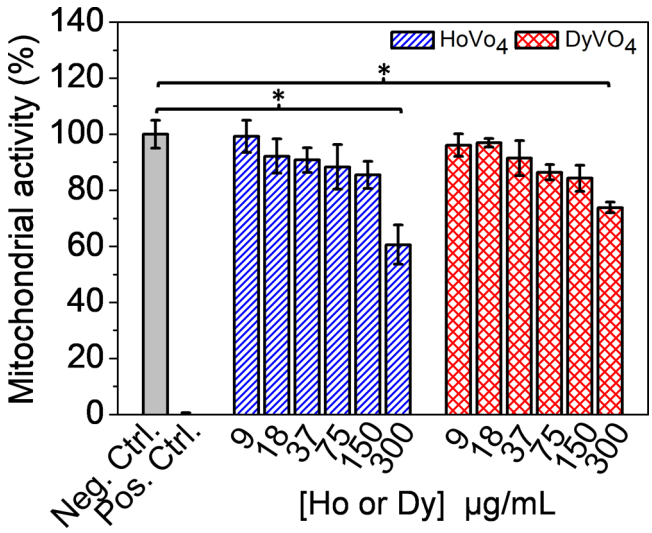

Figure 9. MTT assay of PC3 cells exposed for 24 h to increasing concentration of $HoVO_4$ (blue) and $DyVO_4$ (red) NPs functionalized with PAA. Tested concentrations were from 9 to 300 μg/mL (*, p-value < 0.05).

70% for NPs concentrations up to 150 μg mL^{-1} in the $HoVO_4$ case and even higher concentrations (300 μg mL^{-1}) for the $DyVO_4$ system, indicating negligible toxicity effects under these conditions and therefore their suitability for bioimaging applications.

CONCLUSIONS

We have developed a wet chemical method based on homogeneous precipitation reactions in polyol medium for the synthesis of uniform and well-dispersed $DyVO_4$ and $HoVO_4$ NPs with tetragonal structures, an almost spherical shape, and a mean size of ~60 nm. The surface modification of these NPs with poly(acrylic acid) (PAA) molecules during the synthesis process is needed to render them colloidally stable under physiological pH conditions. It has been found that the transverse relaxivity (r_2) values obtained for both systems at

https://dx.doi.org/10.1021/acs.inorgchem.0c02601
Inorg. Chem. 2021, 60, 152−160

high field (9.4 T) were very high and that the r_2 value of the Dy-based CA was slightly higher (460 M^{-1} s^{-1}) than that of the Ho-based one (424 mM^{-1} s^{-1}), in agreement with the higher magnetization measured for the former, which may be ascribed to its higher magnetic moment. It is worth mentioning that such relaxivity values are the highest so far reported for functionalized Ho- or Dy-based NPs with dimensions below 100 nm, measured at the same magnetic field strength. Both kinds of NPs also show an X-ray attenuation capability superior to that of iohexol, a CT contrast agent commonly used in the clinic. Because of these properties and the rather high biocompatibility of the functionalized NPs, they might be ideal dual probes for high-field MRI and CT bioimaging applications.

AUTHOR INFORMATION

Corresponding Author

Manuel Ocaña − *Instituto de Ciencia de Materiales de Sevilla (CSIC-US), 41092 Sevilla, Spain;* orcid.org/0000-0001-9989-606X; Phone: +34 954489533; Email: mjurado@icmse.csic.es

Authors

Elisabet Gómez-Gónzalez − *Instituto de Ciencia de Materiales de Sevilla (CSIC-US), 41092 Sevilla, Spain*

Nuria O. Núñez − *Instituto de Ciencia de Materiales de Sevilla (CSIC-US), 41092 Sevilla, Spain*

Carlos Caro − *BIONAND, Andalusian Centre for Nanomedicine and Biotechnology (Junta de Andalucía-Universidad de Málaga), 29590 Málaga, Spain; CIBER-BBN, 28029 Madrid, Spain*

Maria L. García-Martín − *BIONAND, Andalusian Centre for Nanomedicine and Biotechnology (Junta de Andalucía-Universidad de Málaga), 29590 Málaga, Spain; CIBER-BBN, 28029 Madrid, Spain;* orcid.org/0000-0002-2257-7682

Yilian Fernández-Afonso − *Instituto de Nanociencia y Materiales de Aragón (INMA), CSIC-Universidad de Zaragoza, 50018 Zaragoza, Spain*

Jesús M. de la Fuente − *CIBER-BBN, 28029 Madrid, Spain; Instituto de Nanociencia y Materiales de Aragón (INMA), CSIC-Universidad de Zaragoza, 50018 Zaragoza, Spain;* orcid.org/0000-0003-1081-8482

Marcin Balcerzyk − *Centro Nacional de Aceleradores (CNA), Universidad de Sevilla, Junta de Andalucía, CSIC, 41092 Sevilla, Spain; Departamento de Fisiología Médica y Bioísica, Facultad de Medicina, Universidad de Sevilla, Sevilla 41009, Spain*

Complete contact information is available at: https://pubs.acs.org/10.1021/acs.inorgchem.0c02601

Notes

The authors declare no competing financial interest.

ACKNOWLEDGMENTS

Funding from FEDER/Ministerio de Ciencia, Innovación y Universidades − Agencia Estatal de Investigación (RTI2018-094426−B-I00 and BIO2017-84246-C2-1-R) and from Gobierno de Aragón (Diputación General de Aragón−Fondo Social Europeo) is acknowledged. Y.F-A. thanks Santander-Universidad Zaragoza fellowship program for her Ph.D. position. We also acknowledge the use of the CNA's ICTS NanoCT facilities and the use of Servicio General de Apoyo a la Investigación-SAI, Universidad de Zaragoza.

REFERENCES

(1) Caravan, P.; Ellison, J. J.; McMurry, T. J.; Lauffer, R. B. Gadolinium(III) Chelates as MRI Contrast Agents: Structure, Dynamics, and Applications. *Chem. Rev.* **1999**, *99*, 2293−2352.

(2) Wang, Y. X. J. Superparamagnetic Iron Oxide Based MRI Contrast Agents: Current Status of Clinical Application. *Quant. Imaging Med. Surg.* **2011**, *1*, 35−40.

(3) Aime, S.; Botta, M.; Terreno, E. Gd (III)-Based Contrast Agents for MRI. *Adv. Inorg. Chem.* **2005**, *57*, 173−237.

(4) Norek, M.; Kampert, E.; Zeitler, U.; Peters, J. A. Tuning of the Size of Dy_2O_3 Nanoparticles for Optimal Performance as an MRI Contrast Agent. *J. Am. Chem. Soc.* **2008**, *130*, 5335−5340.

(5) Rohrer, M.; Bauer, H.; Mintorovitch, J.; Requardt, M.; Weinmann, H. J. Comparison of Magnetic Properties of MRI Contrast Media Solutions at Different Magnetic Field Strengths. *Invest. Radiol.* **2005**, *40*, 715−724.

(6) Norek, M.; Peters, J. A. MRI Contrast Agents Based on Dysprosium or Holmium. *Prog. Nucl. Magn. Reson. Spectrosc.* **2011**, *59*, 64−82.

(7) Hu, F.; Zhao, Y. S. Inorganic Nanoparticle-Based T1 and T1/T2 Magnetic Resonance Contrast Probes. *Nanoscale* **2012**, *4*, 6235−6243.

(8) Barreto, J. A.; O'Malley, W.; Kubeil, M.; Graham, B.; Stephan, H.; Spiccia, L. Nanomaterials: Applications in Cancer Imaging and Therapy. *Adv. Mater.* **2011**, *23*, H18−H40.

(9) Zhang, X.; Blasiak, B.; Marenco, A. J.; Trudel, S.; Tomanek, B.; van Veggel, F. C. J. M. Design and Regulation of $NaHoF_4$ and $NaDyF_4$ Nanoparticles for High-Field Magnetic Resonance Imaging. *Chem. Mater.* **2016**, *28*, 3060−3072.

(10) González-Mancebo, D.; Becerro, A. I.; Rojas, T. C.; García-Martín, M. L.; De la Fuente, J. M.; Ocaña, M. HoF_3 and DyF_3 Nanoparticles as Contrast Agents for High-Field Magnetic Resonance Imaging. *Part. Part. Syst. Charact.* **2017**, *34*, 1700116−1700126.

(11) Lisjak, D.; Plohl, O.; Vidmar, J.; Majaron, B.; Ponikvar-Svet, M. Dissolution Mechanism of Upconverting AYF_4:Yb,Tm (A = Na or K) Nanoparticles in Aqueous Media. *Langmuir* **2016**, *32*, 8222−8229.

(12) Núñez, N. O.; Zambrano, P.; Garcia-Sevillano, J.; Cantelar, E.; Rivera-Fernández, S.; de la Fuente, J. M.; Ocaña, M. Uniform Poly(acrylic acid)-Functionalized Lanthanide-Doped $LaVO_4$ Nanophosphors with High Colloidal Stability and Biocompatibility. *Eur. J. Inorg. Chem.* **2015**, *2015*, 4546−4554.

(13) Nuñez, N. O.; Cussó, F.; Cantelar, E.; Martin-Gracia, B.; de la Fuente, J. M.; Corral, A.; Balcerzyk, M.; Ocaña, M. Bimodal Nd-Doped $LuVO_4$ Nanoprobes Functionalized with Polyacrylic Acid for X-Ray Computed Tomography and NIR Luminescent Imaging. *Nanomaterials* **2020**, *10*, 149−162.

(14) Nuñez, N. O.; Rivera, S.; Alcantara, D.; de la Fuente, J. M.; García-Sevillano, J.; Ocaña, M. Surface Modified Eu:$GdVO_4$ Nanocrystals for Optical and MRI Imaging. *Dalton Trans.* **2013**, *42*, 10725−10734.

(15) Fang, Y. P.; Xu, A. W.; Qin, A. M.; Yu, R. J. Selective Synthesis of Hexagonal and Tetragonal Dysprosium Orthophosphate Nanorods by a Hydrothermal Method. *Cryst. Growth Des.* **2005**, *5*, 1221−1225.

(16) He, H.; Zhang, Y.; Zhu, W.; Zheng, A.; Fang, Z. Controlled Synthesis, Characterization, Mechanism, and Photoluminescence Property of Nanoerythrocyte-Like $HoVO_4$ with High Uniform Size and Morphology. *J. Cryst. Growth* **2011**, *329*, 71−76.

(17) Yang, W.; Xu, L.; Zhai, Z.; Cheng, F.; Yan, Z.; Feng, X.; Zhu, J.; Hou, W. Submicrometer-Sized Hierarchical Hollow Spheres of Heavy Lanthanide Orthovanadates: Sacrificial Template Synthesis, Formation Mechanism, and Luminescent Properties. *Langmuir* **2013**, *29*, 15992−16001.

(18) Lai, H.; Du, Y.; Zhao, M.; Sun, K.; Yang, L. Controlled Synthesis and Luminescent Properties of $DyPO_4$:Eu Nanostructures. *RSC Adv.* **2014**, *4*, 50731−50738.

(19) Khajuria, H.; Kumar, M.; Singh, R.; Ladol, J.; Nawaz Sheikh, H. Additive Assisted Hydrothermal Synthesis, Characterization and Optical Properties of One Dimensional $DyPO_4$:Ce^{3+} Nanostructures. *Solid State Sci.* **2018**, *79*, 58−70.

(20) Bulbul, B.; Beyaz, S. Strong Paramagnetic Crystalline $LnVO_4$ (Ln: Gd, Tb, Dy, Ho, Er) Nanoparticles Synthesized by a Fabricating Method. *Mater. Chem. Phys.* **2016**, *173*, 200−204.
(21) Khorasanizadeh, M. H.; Monsef, R.; Amiri, O.; Amiri, M.; Salavati-Niasari, M. Sonochemical-Assisted Route for Synthesis of Spherical Shaped Holmium Vanadate Nanocatalyst for Polluted Waste Water Treatment. *Ultrason. Sonochem.* **2019**, *58*, 104686.
(22) Mosmann, T. J. Rapid Colorimetric Assay for Cellular Growth and Survival: Application to Proliferation and Cytotoxicity Assays. *J. Immunol. Methods* **1983**, *65*, 55−63.
(23) Kirwan, L. J.; Fawell, P. D.; van Bronswijk, W. In Situ FTIR-ATR Examination of Polyacrylic Acid Adsorbed onto Hematite at Low pH. *Langmuir* **2003**, *19*, 5802−5807.
(24) Gnach, A.; Bednarkiewicz. Lanthanide-Doped Up-Converting Nanoparticles: Merits and Challenges. *Nano Today* **2012**, *7*, 532−563.
(25) González Mancebo, D.; Becerro, A. I.; Corral, A.; Moros, M.; Balcerzyk, M.; de la Fuente, J. M.; Ocaña, M. Enhancing Luminescence and X-ray Absorption Capacity of Eu^{3+}:LaF_3 Nanoparticles by Bi^{3+} Codoping. *ACS Omega* **2019**, *4*, 765−774.
(26) Zhang, Y.; Vijayaragavan, V.; Das, G. K.; Bhakoo, K. K.; Tan, T. T. Y. Single-Phase $NaDyF_4$:Tb^{3+} Nanocrystals as Multifunctional Contrast Agents in High-Field Magnetic Resonance and Optical Imaging. *Eur. J. Inorg. Chem.* **2012**, *2012*, 2044−2048.
(27) Wang, H.; Yi, Z.; Rao, L.; Liu, H.; Zeng, S. High Quality Multi-Functional $NaErF_4$ Nanocrystals: Structure-Controlled Synthesis, Phase-Induced Multi-Color Emissions and Tunable Magnetic Properties. *J. Mater. Chem. C* **2013**, *1*, 5520−5526.
(28) Das, G. K.; Johnson, N. J. J.; Cramen, J.; Blasiak, B.; Latta, P.; Tomanek, B.; van Veggel, F. C. J. M. $NaDyF_4$ Nanoparticles as T2 Contrast Agents for Ultrahigh Field Magnetic Resonance Imaging. *J. Phys. Chem. Lett.* **2012**, *3*, 524−529.

https://dx.doi.org/10.1021/acs.inorgchem.0c02601
Inorg. Chem. 2021, 60, 152−160